Formation of pure zirconium islands inside c-component loops in high-burnup fuel cladding

Journal of Nuclear Materials 597 (2024) 155116

Contents lists available at ScienceDirect

Journal of Nuclear Materials

journal homepage: www.elsevier.com/locate/jnucmat

Short communication

Formation of pure zirconium islands inside c-component loops in high-burnup fuel cladding

David Mayweg [a,*], Johan Eriksson [a,b], Mohammad Sattari [a], Gustav Sundell [a,d], Magnus Limbäck [c], Itai Panas [b], Hans-Olof Andrén [a], Mattias Thuvander [a]

[a] Chalmers University of Technology, Department of Physics, SE-412 96 Göteborg, Sweden
[b] Chalmers University of Technology, Department of Chemistry and Chemical Engineering, SE-412 96 Göteborg, Sweden
[c] Westinghouse Electric Sweden AB, Fuel Materials Innovation, SE-721 63 Västerås, Sweden
[d] Now at ESAB AB, Lindholmsallén 9, SE-417 55 Göteborg, Sweden

GRAPHICAL ABSTRACT

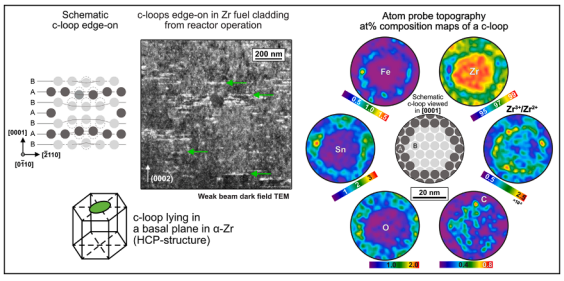

ARTICLE INFO

Keywords:
Nuclear fuel cladding
Zr-alloys
Irradiation-induced damage
Dislocations
Segregation
Atom probe tomography

ABSTRACT

High-burnup Zr-based nuclear fuel claddings exhibit accelerated irradiation growth, corrosion and hydrogen pick-up, all correlated with the emergence of c-component dislocation loops. We made use of sub-nm-resolution atom probe tomography to characterize the nanoscale chemistry of c-loops in fuel cladding from boiling water reactor operation. We found segregation of Fe, Ni and Sn to dislocation lines and depletion of Sn and O inside the loops, resulting in nearly pure Zr islands. We also observed nucleation of suboxide inside one c-loop, pointing to a possible mechanism of accelerated in-reactor corrosion. Such Zr-islands might also promote hydride precipitation and associated degradation.

Fuel rods in water-cooled and -moderated nuclear power reactors comprise zirconium-based cladding in the form of approximately 4 m long tubes that serve as the first containment for the uranium dioxide fuel pellets. The Zr-alloy tubes act as the barrier between fuel and water and conduct the heat from fuel to coolant. Key benefits of Zr are its low capture cross section for thermal neutrons, sufficient mechanical strength and good corrosion properties. Cladding degradation occurs mainly by irradiation damage from fast neutrons, corrosion in water and hydrogen pick-up (HPU). In boiling water reactors (BWRs), Zircaloy-2 and alloys derived from it (HiFi™ [1,2] and Ziron [3]) are used as cladding.

Irradiation damage is caused by fast-neutron-induced collision

* Corresponding author.
E-mail address: david.mayweg@chalmers.se (D. Mayweg).

https://doi.org/10.1016/j.jnucmat.2024.155116
Received 4 March 2024; Received in revised form 12 April 2024; Accepted 20 April 2024
Available online 21 April 2024

Table 1
Chemical composition of the investigated cladding tubes prior to irradiation.

Sample		Fe (%)	Cr (%)	Ni (%)	Sn (%)	O (%)	C (ppm)	Si (ppm)	N (ppm)
KKL	(at%/at ppm)	0.28	0.17	0.08	1.01	0.74	1070	230	320
Zircaloy-2	(wt%/wt ppm)	0.17	0.10	0.05	1.32	0.13	143	70	50
O3	(at%/at ppm)	0.58	0.31	0.097	1.00	0.68	900	290	250
Zircaloy-2 Fe+	(wt%/wt ppm)	0.36	0.18	0.063	1.31	0.12	120	90	38

cascades creating hundreds of vacancies and interstitials. While most defects heal within a short time, permanent defect structures remain and evolve with fluence. Due to the strong texture of the cladding tubes [4–6] and the anisotropic properties of hexagonal close-packed (HCP) α-Zr the emergence of dislocation loops leads to rod-growth in the axial direction [7,8]. Initially, a-type dislocation loops (interstitial and vacancy type) form on close-to-prismatic planes and saturate in number after some time [7,9]. In the a-loop regime growth is moderate, while a marked increase in growth, termed '*breakaway*' coincides with the emergence of vacancy c-component loops (for simplicity hereafter referred to as 'c-loops') [10]. In Zircaloy-2 c-loops are reported to be present from ~ 5 dpa [11–13] without there being evidence for saturation [12,14]. Onset of breakaway growth has been reported to start at 6 dpa [10] and to take place in accelerated form at ~ 11 dpa [15]. Both a- and c-loops have been characterized mostly by transmission electron microscopy (TEM) [7,12,13,16,17] revealing that a-loops (~ 5 nm diameter in one of the investigated materials [18]) align in layers parallel to the basal, i.e. (0001), planes [16,18] and the much larger c-loops lie on basal planes. The c-loop mean diameter for one of the investigated materials is reported to be ~ 100 nm [18]. This assessment was made from edge-on views. Recent TEM imaging has, however, shown that c-loops can have strongly elliptical rather than circular shape [19].

The segregation behavior at dislocation loops has been characterized by TEM using energy-dispersive x-ray spectroscopy (EDX) [19–21]. Segregation patterns of Fe, Cr and Ni, confirming the layered arrangement of clusters, have also been observed in 3D by atom probe tomography (APT) [22–31] that is able to provide elemental characterization on the sub-nm scale [32,33]. It revealed the differing chemistry of clustering at a-loops: in Zircaloy-2 Cr-rich clusters have been observed to be spheroidal, whereas clusters containing only Fe and Ni have been observed to be disk- or ring-shaped. The orientation relationships of cluster layers shown by TEM correspond to those directly determined by APT crystallography [29].

Focused ion beam (FIB) milling at room temperature (RT), which is used for specimen preparation for APT and TEM, is known to cause hydride formation especially for metals with high affinity to H, such as Ti and Zr. However, segregation patterns associated with a-loops are not significantly affected by the α-Zr to δ-hydride (i.e., HCP to face-centered cubic (FCC)) transformation [29] (the layers are then aligned parallel to one set of (111) δ-hydride planes). Around c-loops only Fe and Sn, and very small amounts of Ni, were found at dislocation lines by APT [22]. In Zr-alloys with Sn as the only alloying element a strong increase in c-loop formation and growth with associated irradiation-induced rod growth has been reported [15,28,34]. c-loop formation in Sn-containing alloys can be significantly reduced by addition of Fe and especially Nb (which is not an alloying element in Zircaloy-type alloys) [12,15,34]. Based on density functional theory (DFT) calculations it is expected that stacking faults (SFs) inside c-loops are stabilized by Sn and Fe [35,36].

The corrosion of Zr-alloy fuel cladding results in the formation of zirconia (ZrO_2) and H_2, resulting in an inward-growing oxide scale with initial (approximate) cubic weight gain (in autoclave) [37]. Compared to autoclave in-reactor corrosion is accelerated [37,38]. The acceleration increases with fluence [39]. A further consequence of corrosion is HPU (where a fraction of the H that is produced in the corrosion reaction is absorbed by the Zr metal) [40], which is related to oxidation kinetics and increases with corrosion time [41]. The associated degradation is controlled by H transport through the oxide scale and hydride precipitation. In general, Nb-containing Zr-alloys exhibit lower HPU than Zircaloys [42].

Table 2
Sample information.

	KKL	O3
Heat treatment code	*Westinghouse* LK3 [65]	*Westinghouse* LK3 [65]
Irradiation time	9 annual cycles (2970 days)	2082 days
Rod average burn-up (MWd/kgU)	79 [44]	52 [25]
Elevation from rod bottom (mm)	2100	2666–2669
Fast neutron fluence (n m^{-2})	1.8×10^{26}	1.2×10^{26}
Damage level (dpa) [45]	29	19
Oxide thickness (μm)	45 ± 7 Eddy current 46 ± 2.5 Metallographic cross section [44]	11 ± 2 Eddy current 9.8 ± 0.6 (FIB cross section)
Rod growth	28.5 mm (~ 0.71%) [46]	0.38%
Hydrogen concentration post-irradiation (wt ppm/ at%)	664 ± 94/ ~ 6	134 ± 9/ ~ 1.2

Table 3
Experimental parameters used in the APT analyses.

	KKL	**O3**
APT system	*LEAP 3000X HR*	*LEAP 6000XR*
Laser wavelength (nm)	532	257.5
Laser pulse energy (pJ)	250	50–70
Base temperature (K)	70	50–60
Specimen preparation	FIB (RT)	FIB (cryo, annular milling at –150 °C)
Analyzed phase	δ-hydride (FIB-induced)	α-Zr

We investigated samples taken from two fuel cladding tubes from BWRs in Switzerland (Kernkraftwerk Leibstadt – KKL) and Sweden (Oskarshamn 3 – O3). Both were produced by Sandvik Materials Technology AB (now Alleima AB) and operated in fuel assemblies manufactured by Westinghouse Electric Sweden AB. Investigations of the same samples have been published previously: KKL see references 36–53 in [24]; O3 see [25,29,31]. The compositions prior to operation are given in Table 1. The cladding irradiated in O3 was a modified Zircaloy-2 with higher Fe concentration than Zircaloy-2 [43]. It is close to the specifications for HiFi (Cr is slightly higher at 0.17 wt% vs. 0.05–0.15 wt% [2]); here we use the designation '*Zircaloy-2 Fe+*' (as opposed to '*Alloy 2*' in [29]). Information about the conditions of the fuel rods after irradiation are given in Table 2.

We analyzed legacy APT data sets from the KKL tube (partially published in [22–24] obtained with an *Imago LEAP 3000X HR)* in more detail, and we conducted further APT experiments on specimens from the O3 tube using a *Cameca LEAP 6000XR*. The relevant experimental information, including APT parameters, is listed in Table 3.

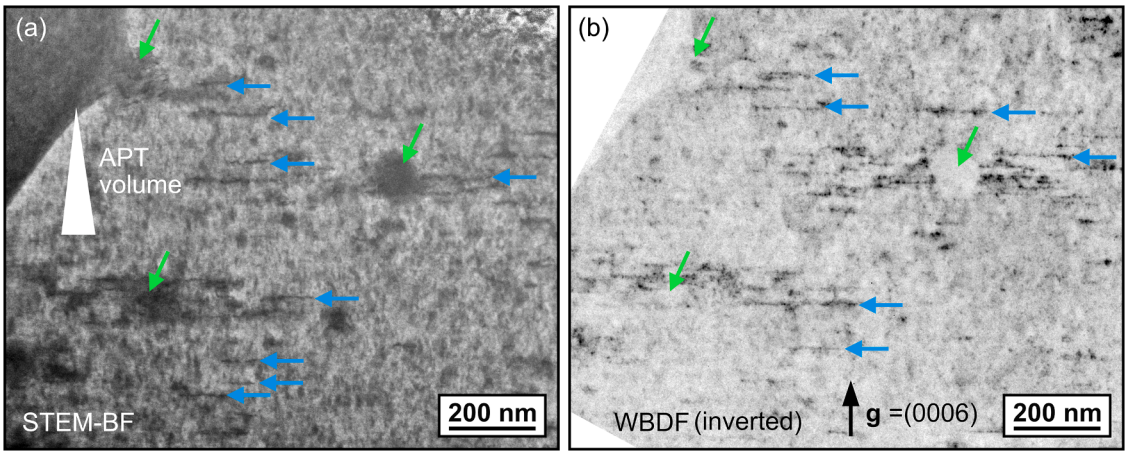

Fig. 1. TEM images of assumed c-loops in Zircaloy-2 Fe+, (a) STEM bright-field and (b) inverted weak-beam dark-field (WBDF) image using the (0006) reflection. c-loops and SPPs highlighted by blue and green arrows respectively.

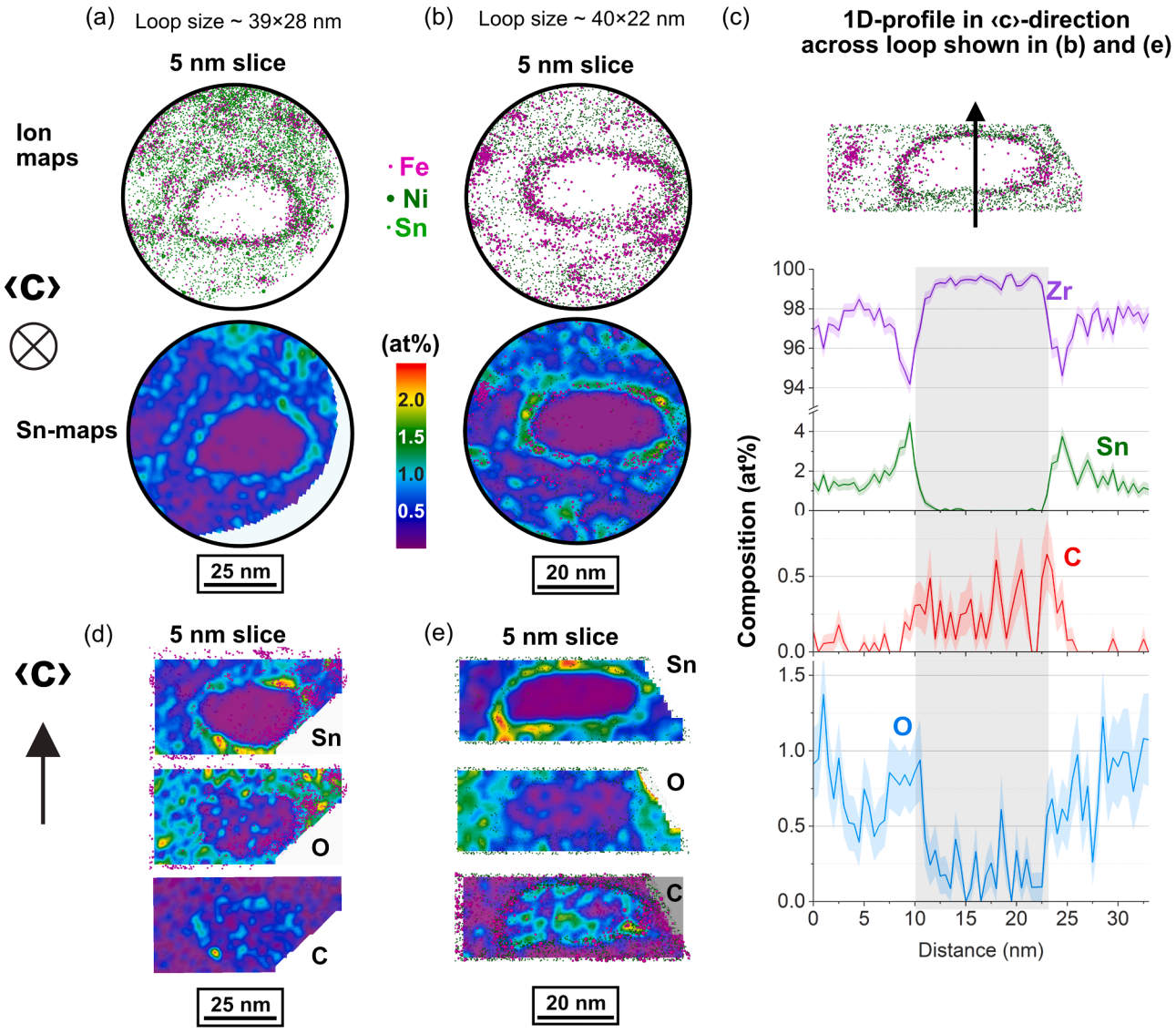

Fig. 2. c-loops exhibiting rejection of O and Sn and C-partitioning to the SF inside the dislocation loop (KKL tube, LEAP 3000X HR, RT-FIBed, 250 pJ, 70 K). (a) and (b) are views on the basal plane, (d) and (e) perpendicular to it. (c) 1D composition profile across the SF in c-direction for the loop in (b) and (e).

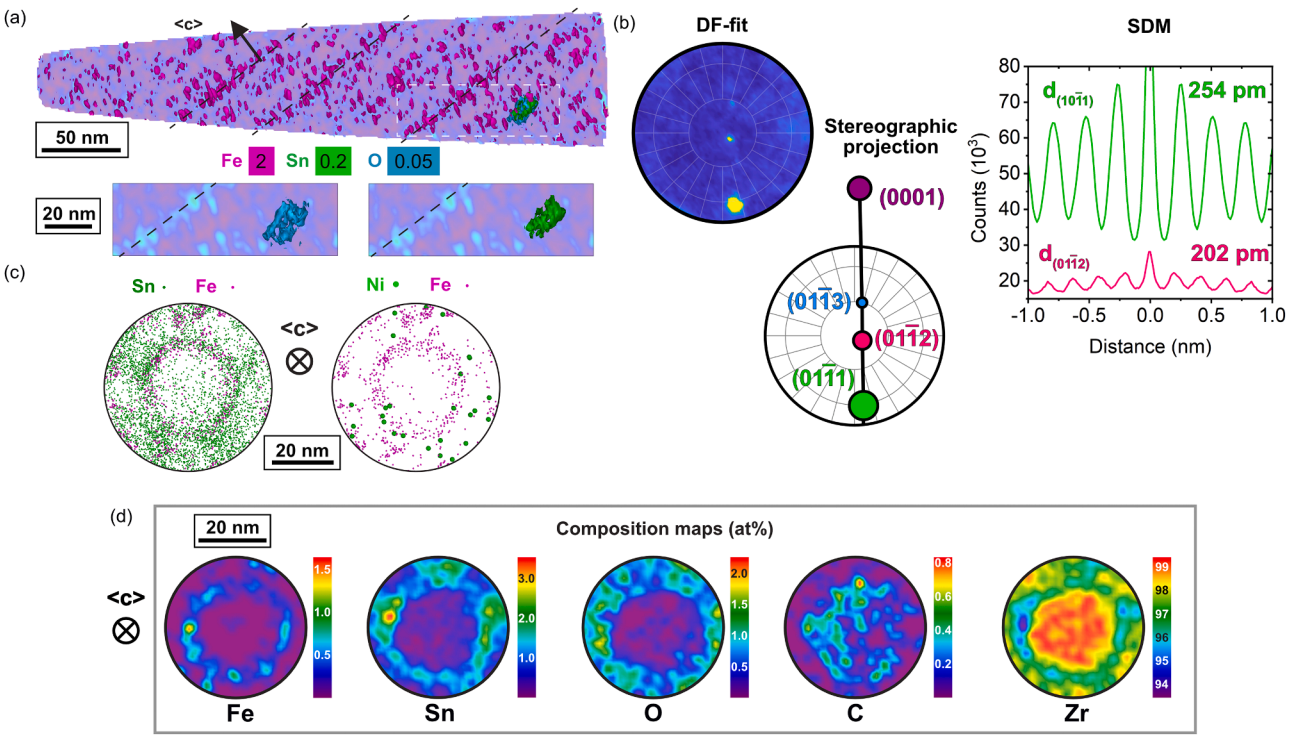

Fig. 3. Reconstruction of a data set from the O3 tube (LEAP 6000XR, cryo-FIB, 60pJ, 60 K). (a) position of the loop 'edge-on' (see O and Sn ICSs with values of 0.05 and 0.2 at%, respectively) in a volume with layered a-loop clusters (Fe ICS 2 at%). (b) crystallographic analysis. (c) Fe, Ni and Sn are segregated to the dislocation line. (d) Composition maps from 5 nm slices with view in the c-direction.

Reconstructions and analyses were made in *IVAS 3.6.14* and *AP Suite 6.3*. We initially ranged all H-containing molecular species (H^+, H_2^+, ZrH^{++}, ZrH^{+++}, $Zr_2H_3^{+++}$and additional minor species) but could not identify any relevant H-related features at or around what we identified as c-loops. And, since most H in the APT data is either an artifact from specimen preparation or originates from the analysis chamber, H was then excluded from further analyses. We used *MATLAB* scripts from Breen et al. [47] to reveal the latent crystallographic features present in the data sets to first obtain the crystallographic orientation of the specimens and then calibrate the data sets [48]. We used an *FEI Titan 80–300* for conventional and scanning TEM (STEM). For details of the APT specimen preparation from the KKL tube see [22]. Lift-outs for APT and TEM from the O3 tube were performed in an *FEI Versa 3D* FIB instrument. Annular milling for APT [49] and thinning for TEM was performed at cryogenic temperature ('*cryo-FIB*'; stage temperature was below –150 °C, cold-trap around –180 °C) in a *Tescan GAIA3* equipped with a *Leica VCT-500* cryo-stage to avoid a transformation of α-Zr into δ-hydride [29,50–52].

Fig. 1 shows TEM images of a foil from the O3 tube oriented near a two-beam condition highlighting c-loops (zone axis close to [01 $\bar{}$ 10]). Second phase particles (SPPs) [53] are marked by green and c-loops by blue arrows. Fig. 1(a) is a STEM bright field image. The schematic depiction of a 300 nm long APT specimen shows that the probability of capturing c-loops within the volume is relatively low. The contrast in the (inverted, see also Fig. S1) weak-beam dark-field (WBDF) image in (b) highlights slightly different features. Note, that image quality and contrast are inferior compared to some foils prepared by electro-polishing [16,18,21], which is likely owed to larger thickness.

In our APT data we found a total of nine features we identified as c-loops: five in the KKL (8 runs $> 10 \times 10^6$ ions) and four in the O3 tube (14 runs $> 2 \times 10^6$ ions). These features were identified based on circular or elliptical line-segregation patterns of alloying elements that have been consistently identified as dislocation loops by APT in other systems [54–56]. Sawabe et al. [27] have shown ring-shaped structures of Fe and Ni, which constitute segregation to a-loops (as has been predicted by simulations [57,58]). We therefore assume that the observed segregation at ring-shaped features in our data represent dislocation loops (although they are not resolved structurally in the present data). All loops are lying on basal planes whose orientations were identified based on APT crystallography *and* a-loop-associated cluster layers. We used the DF-fit algorithm [59] to reveal latent lattice periodicity in laser-pulsing APT data where crystallographic information is often not clearly visible. The loops we found by APT were mostly significantly smaller than the reported mean size of ~ 100 nm from TEM of the KKL tube [18] and are also mostly elliptical (major/minor axes = 52±24 nm/34±11 nm, see Fig. S1 and Table S1).

Fig. 2 depicts two c-loops from a data set obtained from RT-FIB-milled α-Zr (high measured H fraction indicates α→δ transformation) with a view in the c-direction ((a), (b)) and perpendicular to it ((d), (e)). Both loops exhibit Fe and Sn segregation to the dislocation line. Inside the two loops in Fig. 2 we found rejection of all elements (except C) from the SF-plane. This means that nearly pure Zr is present here. Noteworthy is that small amounts of the trace element C (detected as C^+, CH^+ and ZrC^{++}) are present. The view perpendicular to the c-direction ('edge-on' like in the TEM image in Fig. 1) shows that this pure-Zr volume is of ellipsoidal shape, i.e., all alloying elements are rejected within the basal plane as well as in the c-direction ('above and below' the SF). Fig. 2(c) shows concentration profiles across the c-loop in (b) and (e) to highlight the striking fact that the region above and below the SF is virtually Sn-free, only containing Zr, < 0.5 at% C and very little O.

Fig. 3(a) depicts a reconstruction of a specimen from the O3 tube where the annular milling was carried out at cryogenic temperature to prevent the α→δ transformation, i.e., this data set was obtained from an α-Zr specimen. The 2 at% Fe isoconcentration surface (ICS) and dashed lines show the typical layered arrangement of Fe-rich a-loops parallel to basal planes. A 0.05 at% O and a 0.2 at% Sn ICS (lower concentration inside) highlight the position of a c-loop that is viewed edge-on (see also enlarged views of the region inside the dashed rectangle). Fig. 3(b) shows results from the crystallographic analysis; the field evaporation image (FEI), the stereographic projection with three indexed poles and

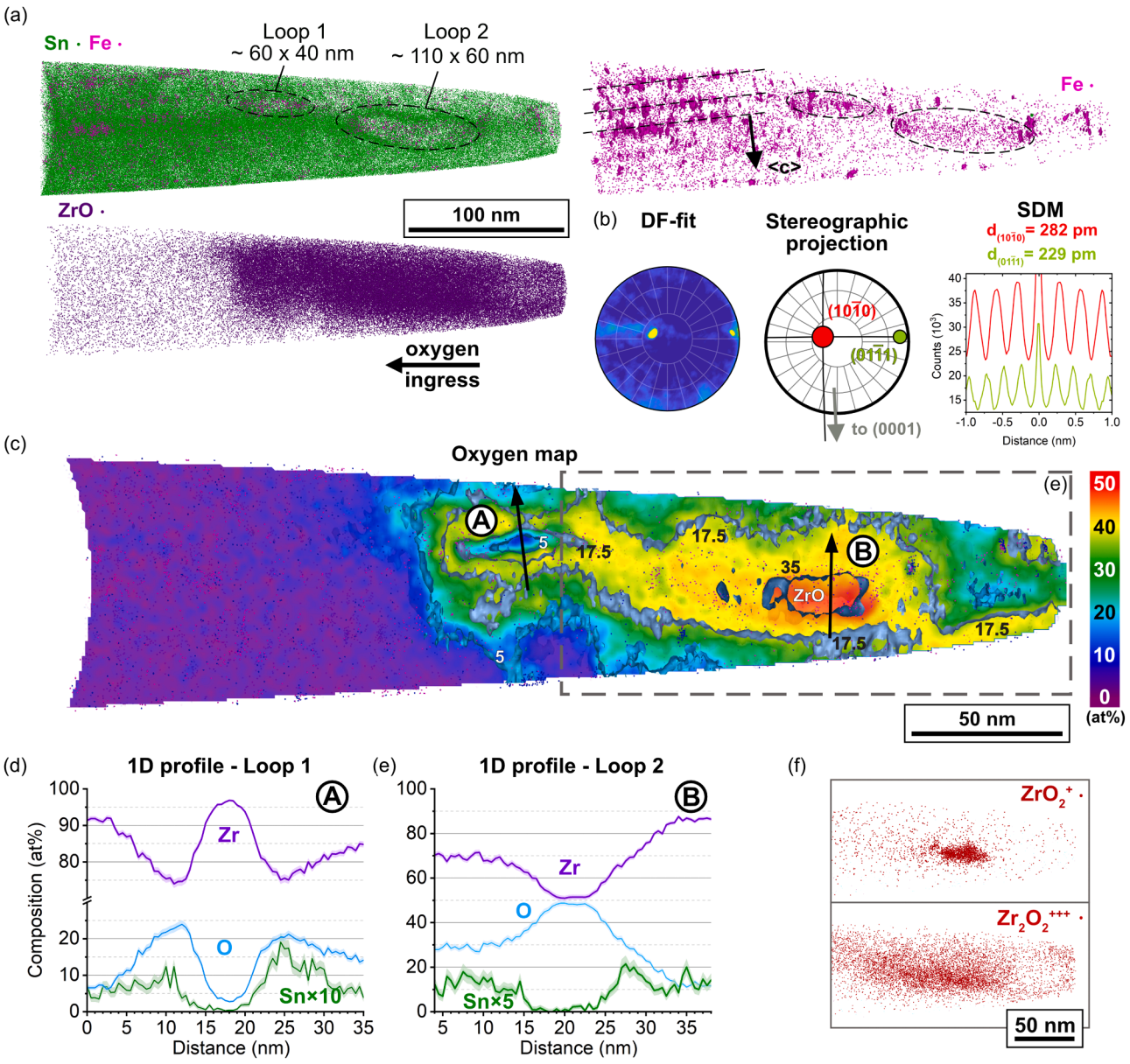

Fig. 4. Internal oxidation at c-loops in the metal close to the oxide-metal interface in the O3 tube (LEAP 6000XR, cryo-FIB, 70 pJ, 50 K). (a) Ion maps of Sn and Fe (including a 1 at% ICS) and of $ZrO^{+/++}$. (b) Depiction of crystallographic information contained in the data set. (c) A map of the O fraction in a 10 nm slice across the reconstruction. (d) and (e) 1D composition profiles across the loops shown in (a) and (b). (f) The distribution of the molecular ions ZrO_2^+ and $Zr_2O_2^{+++}$ inside Loop 2.

the spatial distribution maps (SDMs) [60] for the $(01\bar{1}1)$, and $(01\bar{1}2)$, planes. The measured lattice spacings deviate only slightly from the theoretical values ($d_{(01\bar{1}1)m}$ = 254 pm vs. $d_{(01\bar{1}1)th}$= 246 pm and $d_{(01\bar{1}2)m}$ = 202 pm vs. $d_{(01\bar{1}2)th}$= 189 pm), thus confirming the correct indexing. The assumed position of the (0001) pole fits well with the observed angle of the basal plane orientation based on cluster layers in Fig. 3(a). The ion maps in Fig. 3(c) and concentration maps in Fig. 3(d) show the same segregation pattern as the loops in Fig. 2: Sn and Fe (maybe also Ni) are segregated to the dislocation line, and all alloying elements are rejected from the SF. We construe the similarity with Fig. 2 as evidence that the distribution of alloying and trace elements is not affected by FIB-induced α→δ transformation, like in the case of clusters around a-loops [29]. The concentration maps in Fig. 3(c) showcase that the region inside the c-loop is nearly pure Zr, again containing small amounts of C. We hence propose that the c-loops presented in Figs. 2 and 3 (located in α-Zr containing Fe and Ni, but not Cr) are representative of c-loops in such environments, i.e., they constitute virtually pure Zr islands inside the bulk of alloyed Zr-based cladding.

The Sn and Fe (and Ni) segregation to the dislocation line is in agreement with predictions from forcefield simulations with parameters determined from DFT calculations [61]. However, the rejection of Sn from the SF (or the expected approximately ellipsoidal strain field around it [35,62]) seems to be contradicting what is reported from simulations [35]. The existence of a second phase is unlikely since the Sn fraction surrounding the Sn-free region is not exceeding the solubility limit of ~ 4 at% at operating temperature (~ 300 °C) [61,63]. O depletion has also not been predicted by simulations [35]. In general, alloying has been shown to affect c-loop formation [15,17,36,64] but no mechanism resembling our observations is known. Interstitial impurities such as C, N[1] and O have been linked to c-loop formation ([8, 66] and references therein), especially C is associated with accelerated growth

[1] Due to a peak overlap with Si, N is largely 'invisible' in our APT data since both N and Si are only present in low concentrations.

[65] but here, too, exists no understanding of the underlying mechanism (s).

The reconstruction displayed in Fig. 4 originates from a lift-out close to the oxide-metal interface in the O3 tube, prepared by annular milling under cryogenic conditions. The ion maps in Fig. 4(a) (see Figure S3 for more views) show two distinct Sn- and Fe-related features that resemble c-loops in Fig. 2 and Figure 3; the O ingress from the oxide is visualized by display of $ZrO^{+/++}$ ions. The layers associated with a-loops in the Fe map reveal the <*c*>-direction, showing that their crystallographic orientation fits with what is expected for c-loops (for a view in the c-direction, see Figure S3). Fig. 4(b) depicts results from the crystallographic analysis: the FEI, the stereographic projection with two poles each and SDMs for the $(10\bar{1}0)$, and $(01\bar{1}1)$ planes. The measured lattice spacings again deviate only slightly from the theoretical values ($d_{(10\bar{1}0)m}$ = 282 pm vs $d_{(10\bar{1}0)th}$= 280 pm and $d_{(01\bar{1}1)m}$ = 229 pm vs $d_{(01\bar{1}1)th}$= 246 pm). The assumed position of the (0001) pole fits well with the observed angle of the basal plane orientation based on cluster layers highlighted in the Fe ion map in Fig. 4(a).

The segregation pattern of both loops in Fig. 4 is essentially the same as in the c-loops shown in the previous figures: Sn is clearly removed from an ellipsoidal volume inside the loop (see Sn map in Fig. 4(a)), while both Fe and Sn segregate to the dislocation line. In Fig. 4(c) it is shown that Loop 1 is surrounded by O levels close to saturation in Zr (~ 29 at% [66]), while the O fraction inside the loop is much lower. A possible cause is the 'Sn shell' acting as a barrier that has to be penetrated by O. This is also evident from the 1D profile through the inside of the loop (see arrow 'A' pointing in the c-direction) depicted in Fig. 4(c). Like in the loops shown previously, here, too, the center of the loop is virtually Sn-free. Inside Loop 2, which is closer to the oxide-metal interface, nucleation of suboxide (composition ZrO – red in the O map in Fig. 4(c)) took place. This distinct phase has been observed at interfaces between zirconia and metal in Zircaloys [67–69]. This is further illustrated in the concentration profile (see Fig. 4(c) arrow 'B') in Fig. 4(e). Again, a largely Sn-free region is found that has a Zr:O ratio of approximately 1:1. Further evidence for the presence of suboxide is given in Fig. 4(f): molecular ionic species[2] (ZrO_2^+, $Zr_2O_2^{+++}$) are absent in O-saturated Zr, but have been shown to correlate with the suboxide phase [68]. In distinction, O_2^+ ions are found in zirconia but not here (or in larger suboxide volumes). While this appears to be a practical way of distinguishing these phases their presence is not a direct property of the respective phase, but rather depend on the (local) field strength (which can vary strongly especially at phase or grain boundaries). We construe these findings as a potential internal oxidation mechanism that could contribute to an acceleration of corrosion at high fluence. Furthermore, such accelerated corrosion has been linked to the presence of C [70], whose role might be clarified by the finding that C is present in the pure Zr islands inside c-loops (as shown in Figs. 2 and 3).

Our APT data from different instruments, different cladding tubes and different FIB-preparation routes have presented consistent evidence that inside c-loops in Zircaloy-2 type cladding the formation of virtually unalloyed Zr islands takes place. These essentially pure Zr volumes and the strong rejection of Sn have to be viewed in the light of the evidence of a strong correlation between Sn concentration and the emergence of c-loops [15,36].

In addition to the relation with growth and corrosion such pure Zr islands might be relevant for HPU in general and hydride nucleation in particular. Since almost all alloying elements (Fe, Cr, Ni, Sn, O) destabilize hydrides [61] the virtually de-alloyed Zr inside c-loops could accelerate HPU by promoting hydride nucleation at c-loops (especially hydride rims [71]). Although a challenging experimental approach, gaseous deuterium-charging of APT specimens (to circumvent the limited H detection capabilities of APT) could be performed in future work in order to identify if pure Zr islands act as trapping sites [72–74]. This is of interest because H is related to significantly increased irradiation-induced growth [75].

To better understand the role of Sn, simulation studies that take our experimental findings into account should be considered. And, since there is a significant effect of Nb (and to a lesser extent Fe) in reducing irradiation-induced growth [15], it would be ideal to perform APT of c-loops from irradiated Zr-Nb-alloys to be able to elucidate the potential interplay of Nb (and/or Fe) and Sn.

[2] These are not compounds but ions with more than one atom that are formed by co-evaporation of more than a single atom.

CRediT authorship contribution statement

David Mayweg: Writing – review & editing, Writing – original draft, Visualization, Validation, Investigation, Formal analysis, Conceptualization. **Johan Eriksson:** Writing – review & editing, Investigation, Conceptualization. **Mohammad Sattari:** Writing – original draft, Investigation. **Gustav Sundell:** Writing – review & editing, Investigation, Formal analysis. **Magnus Limbäck:** Writing – review & editing, Resources. **Itai Panas:** Writing – review & editing, Conceptualization. **Hans-Olof Andrén:** Writing – review & editing, Conceptualization. **Mattias Thuvander:** Writing – review & editing, Supervision, Funding acquisition, Conceptualization.

Declaration of competing interest

The authors declare that they have no known competing financial interests or personal relationships that could have appeared to influence the work reported in this paper.

Data availability

Data will be made available on request.

Acknowledgments

DM gratefully acknowledges funding from the Swedish Centre for Nuclear Technology (SKC). We acknowledge OKG, Vattenfall, Westinghouse and EPRI for financial support. The authors thank Pia Tejland at Studsvik for provision of the cladding tube samples and performing some of the FIB lift-outs from the KKL material. The MUZIC and MIDAS communities are recognized for fruitful collaboration. All APT and TEM experiments were performed at Chalmers Materials Analysis Laboratory (CMAL).

Supplementary materials

Supplementary material associated with this article can be found, in the online version, at doi:10.1016/j.jnucmat.2024.155116.

References

[1] K. Kakiuchi, K. Ohira, N. Itagaki, Y. Otsuka, Y. Ishii, A. Miyazaki, Irradiated behavior at high burnup for HiFi alloy, J. Nucl. Sci. Technol. 43 (9) (2006) 1031–1036.
[2] J.M. Wright, M. Limbäck, D. Schrire, M. Owaki, M. Nilsson, Commercial Introduction and Experience with the Advanced High Iron Cladding HIFI® in Boiling Water Reactors, TopFuel, Prague, 2018, p. A0101.
[3] K. Une, K. Sakamoto, M. Aomi, J. Matsunaga, Y. Etoh, I. Takagi, S. Miyamura, T. Kobayashi, K. Ito, Hydrogen absorption mechanism of zirconium alloys based on characterization of oxide layer, in: P. Barbéris, M. Limbäck (Eds.), ASTM International, West Conshohocken, PA, 2012, pp. 401–432.
[4] C. Lemaignan, A.T. Motta, Zirconium alloys in nuclear applications, in: R.W. Cahn, P. Haasen, E.J. Kramer (Eds.), Materials Science and Technology,, 2006.
[5] B.A. Cheadle, C.E. Ells, W. Evans, The development of texture in zirconium alloy tubes, J. Nucl. Mater. 23 (2) (1967) 199–208.
[6] E. Tenckhoff, P. Rittenhouse, The influence of the reduction values on texture formation in zircaloy tubing produced with low deformations, Int. J. Mater. Res. 63 (2) (1972) 83–88.

[7] G.J.C. Carpenter, D.O. Northwood, The contribution of dislocation loops to radiation growth and creep of Zircaloy-2, J. Nucl. Mater. 56 (1975) 260–266.
[8] M. Griffiths, Irradiation growth, Compreh. Nucl. Mater. (2020) 367–405.
[9] M. Griffiths, A review of microstructure evolution in zirconium alloys during irradiation, J. Nucl. Mater. 159 (1988) 190–218.
[10] A. Rogerson, R.A. Murgatroyd, Breakaway' growth in annealed Zircaloy-2 at 353 K and 553 K, J. Nucl. Mater. 113 (2) (1983) 256–259.
[11] R.W. Gilbert, R.A. Holt, Dislocation structure in neutron irradiated zircaloy, J. Nucl. Mater. 102 (1) (1981) 1–6.
[12] R.A. Holt, R.W. Gilbert, V. Fidleris, Dislocation Substructure in Zirconium Alloys Irradiated in EBR-II, in: J.S. Perrin (Ed.), Effects of Radiation on Materials, ASTM International, West Conshohocken, PA, 1982, pp. 234–250.
[13] D.O. Northwood, R.W. Gilbert, L.E. Bahen, P.M. Kelly, R.G. Blake, A. Jostsons, P. K. Madden, D. Faulkner, W. Bell, R.B. Adamson, Characterization of neutron irradiation damage in zirconium alloys — An international "round-robin" experiment, J. Nucl. Mater. 79 (2) (1979) 379–394.
[14] R.A. Holt, R.W. Gilbert, ⟨c⟩ Component dislocations in annealed Zircaloy irradiated at about 570 K, J. Nucl. Mater. 137 (3) (1986) 185–189.
[15] S. Yagnik, R. Adamson, G. Kobylyansky, J.-H. Chen, D. Gilbon, S. Ishimoto, T. Fukuda, L. Hallstadius, A. Obukhov, S. Mahmood, Effect of alloying elements, cold work, and hydrogen on the irradiation-induced growth behavior of zirconium alloy variants, in: R.J. Comstock, A.T. Motta (Eds.), Zirconium in the Nuclear Industry: 18th International Symposium, ASTM International, West Conshohocken, PA, 2018, pp. 748–795.
[16] A. Jostsons, P.M. Kelly, R.G. Blake, The nature of dislocation loops in neutron irradiated zirconium, J. Nucl. Mater. 66 (3) (1977) 236–256.
[17] A. Jostsons, P.M. Kelly, R.G. Blake, K. Farrell, Neutron Irradiation-Induced Defect Structures in Zirconium, in: D. Kramer (Ed.), Effects of Radiation on Structural Materials, ASTM International, West Conshohocken, PA, 1979, pp. 46–61.
[18] A. Harte, D. Jädernäs, M. Topping, P. Frankel, C.P. Race, J. Romero, L. Hallstadius, E.C. Darby, M. Preuss, The effect of matrix chemistry on dislocation evolution in an irradiated Zr alloy, Acta Mater. 130 (2017) 69–82.
[19] Z. Wang, Z.Q. Fang, Q.X. Yan, L. Wu, C.Y. Lu, TEM Investigation on the Dislocation Loops in Zirconium Alloy By Neutron and Kr+ Ion Irradiation Tests, Microscopy and microanalysis: the Official Journal of Microscopy Society of America, Microbeam Analysis Society, Microscopical Society of Canada, 2024.
[20] A. Harte, M. Topping, P. Frankel, D. Jädernäs, J. Romero, L. Hallstadius, E. C. Darby, M. Preuss, Nano-scale chemical evolution in a proton-and neutron-irradiated Zr alloy, J. Nucl. Mater. 487 (2017) 30–42.
[21] Y. de Carlan, C. Regnard, M. Griffiths, D. Gilbon, C. Lemaignan, Influence of iron in the nucleation of ⟨c⟩ component dislocation loops in irradiated zircaloy-4, in: E. R. Bradley, G.P. Sabol (Eds.), Zirconium in the Nuclear Industry: Eleventh International Symposium, ASTM International, West Conshohocken, PA, 1996, pp. 638–653.
[22] G. Sundell, M. Thuvander, P. Tejland, M. Dahlbäck, L. Hallstadius, H.-O. Andrén, Redistribution of alloying elements in Zircaloy-2 after in-reactor exposure, J. Nucl. Mater. 454 (1–3) (2014) 178–185.
[23] J. Eriksson, G. Sundell, P. Tejland, H.-O. Andrén, M. Thuvander, An atom probe tomography study of the chemistry of radiation-induced dislocation loops in Zircaloy-2 exposed to boiling water reactor operation, J. Nucl. Mater. 550 (2021) 152923.
[24] J. Eriksson, G. Sundell, P. Tejland, H.-O. Andrén, M. Thuvander, Nanoscale chemistry of Zircaloy-2 exposed to three and nine annual cycles of boiling water reactor operation — an atom probe tomography study, J. Nucl. Mater. 561 (2022) 153537.
[25] J. Eriksson, Evolution of Microstructure and Nanoscale Chemistry of Zircaloy-2-type alloys During Nuclear Reactor operation, Department of Physics, Chalmers University of Technology, 2022.
[26] T. Sawabe, T. Sonoda, Evolution of nanoscopic iron clusters in irradiated zirconium alloys with different iron contents, J. Nucl. Sci. Technol. 55 (10) (2018) 1110–1118.
[27] T. Sawabe, T. Sonoda, An atom probe study on the Fe distribution in Zr-based alloys with different Fe content under high fluence neutron irradiation, J. Nucl. Mater. 567 (2022) 153809.
[28] R.H. Zee, A. Rogerson, G.J.C. Carpenter, J. Watters, Effect of tin on the irradiation growth of polycrystalline zirconium, J. Nucl. Mater. 120 (2) (1984) 223–229.
[29] D. Mayweg, J. Eriksson, O. Bäcke, A.J. Breen, M. Thuvander, Focused Ion Beam induced hydride formation does not affect Fe, Ni, Cr-clusters in irradiated Zircaloy-2, J. Nucl. Mater. 581 (2023) 154444.
[30] B.M. Jenkins, J. Haley, M.P. Moody, J.M. Hyde, C.R.M. Grovenor, APT and TEM study of behaviour of alloying elements in neutron-irradiated zirconium-based alloys, Scr. Mater. 208 (2022) 114323.
[31] J. Eriksson, D. Mayweg, G. Sundell, H.-O. Andrén, M. Thuvander, Solute concentrations in the matrix of zirconium alloys studied by atom probe tomography, in: S.K. Yagnik, M. Preuss (Eds.), ASTM STP 1645, Ottawa, 2023, pp. 149–172.
[32] B. Gault, A. Chiaramonti, O. Cojocaru-Mirédin, P. Stender, R. Dubosq, C. Freysoldt, S.K. Makineni, T. Li, M. Moody, J.M. Cairney, Atom probe tomography, Nat. Rev. Method. Prim. 1 (1) (2021) 51.
[33] D.N. Seidman, K. Stiller, An atom-probe tomography primer, MRS Bull. 34 (10) (2009) 717–724.
[34] E. Francis, R.P. Babu, A. Harte, T.L. Martin, P. Frankel, D. Jädernäs, J. Romero, L. Hallstadius, P.A.J. Bagot, M.P. Moody, M. Preuss, Effect of Nb and Fe on damage evolution in a Zr-alloy during proton and neutron irradiation, Acta Mater. 165 (2019) 603–614.
[35] J.F. March-Rico, G. Huang, B.D. Wirth, The effect of local chemical environment on the energetics of stacking faults and vacancy platelets inα-zirconium, J. Nucl. Mater. 540 (2020) 152339.
[36] J. Hu, Q. Lv, W. Lin, Short communication: effect of Sn on the formation of <c>-component dislocation loops in Zr alloys: in situ ion irradiation studies and atomistic simulations, J. Nucl. Mater. 587 (2023).
[37] B. Cox, Some thoughts on the mechanisms of in-reactor corrosion of zirconium alloys, J. Nucl. Mater. 336 (2005) 331–368.
[38] E. Hillner, D.G. Franklin, J.D. Smee, Long-term corrosion of Zircaloy before and after irradiation, J. Nucl. Mater. 278 (2) (2000) 334–345.
[39] B.C. Cheng, R.M. Kruger, R.B. Adamson, Corrosion behavior of irradiated zircaloy, in: A.M. Garde, E.R. Bradley (Eds.), Zirconium in the Nuclear Industry: Tenth International Symposium, ASTM International, West Conshohocken, PA, 1994, pp. 400–418.
[40] A.T. Motta, A. Couet, R.J. Comstock, Corrosion of zirconium alloys used for nuclear fuel cladding, Annu. Rev. Mater. Res. 45 (1) (2015) 311–343.
[41] A.T. Motta, L. Capolungo, L.-Q. Chen, M.N. Cinbiz, M.R. Daymond, D.A. Koss, E. Lacroix, G. Pastore, P.-C.A. Simon, M.R. Tonks, B.D. Wirth, M.A. Zikry, Hydrogen in zirconium alloys: a review, J. Nucl. Mater. 518 (2019) 440–460.
[42] A. Couet, A.T. Motta, R.J. Comstock, Hydrogen pickup measurements in zirconium alloys: relation to oxidation kinetics, J. Nucl. Mater. 451 (1) (2014) 1–13.
[43] Standard Specification for Zirconium and Zirconium Alloy Ingots for Nuclear Application Standard B350/B350M - 11, ASTM, 2021, p. e1.
[44] J. Romero, L. Hallstadius, M. Owaki, G. Pan, K. Kataoka, K. Kakiuchi, R. J. Comstock, J. Partezana, A. Mueller, M. Dahlbäck, A. Garde, A. Atwood, M. Åslund, Evolution of westinghouse fuel cladding, in: Proceedings of WRFPM/TopFuel, Sendai, Japan, 2014.
[45] S. Abolhassani, A. Baris, R. Grabherr, J. Hawes, A. Colldeweih, R. Vanta, R. Restani, A. Hermann, J. Bertsch, M. Chollet, G. Kuri, M. Martin, S. Portier, H. Wiese, H. Schweikert, G. Bart, K. Ammon, G. Ledergerber, M. Limbäck, Toward an improved understanding of the mechanisms involved in the increased hydrogen uptake and corrosion at high burnups in zirconium based claddings, in: A.T. Motta, S.K. Yagnik (Eds.), Zirconium in the Nuclear Industry: 19th International Symposium, ASTM International, West Conshohocken, PA, 2021, pp. 435–466.
[46] L. Walters, S.R. Douglas, M. Griffiths, Equivalent radiation damage in zirconium irradiated in various reactors, ASTM STP 1597 (2018) 676–690.
[47] S. Valizadeh, G. Ledergerber, S. Abolhassan, D. Jädernäs, M. Dahlbäck, E. Mader, G. Zhou, J. Wright, L. Hallstadius, Effects of secondary phase particle dissolution on the in-reactor performance of BWR cladding, J. ASTM. Int. 8 (2) (2011) 1–16.
[48] A.J. Breen, A.C. Day, B. Lim, W.J. Davids, S.P. Ringer, Revealing latent pole and zone line information in atom probe detector maps using crystallographically correlated metrics, Ultramicroscopy. 243 (2023) 113640.
[49] B. Gault, D. Haley, F. de Geuser, M.P. Moody, E.A. Marquis, D.J. Larson, B. P. Geiser, Advances in the reconstruction of atom probe tomography data, Ultramicroscopy 111 (6) (2011) 448–457.
[50] K. Thompson, D. Lawrence, D.J. Larson, J.D. Olson, T.F. Kelly, B. Gorman, In situ site-specific specimen preparation for atom probe tomography, Ultramicroscopy 107 (2–3) (2007) 131–139.
[51] I. Mouton, A.J. Breen, S. Wang, Y. Chang, A. Szczepaniak, P. Kontis, L. T. Stephenson, D. Raabe, M. Herbig, T.B. Britton, B. Gault, Quantification challenges for atom probe tomography of hydrogen and deuterium in zircaloy-4, Microsc. Microanaly. 25 (2) (2019) 481–488.
[52] Y.H. Chang, I. Mouton, L. Stephenson, M. Ashton, G.K. Zhang, A. Szczpaniak, W. J. Lu, D. Ponge, D. Raabe, B. Gault, Quantification of solute deuterium in titanium deuteride by atom probe tomography with both laser pulsing and high-voltage pulsing: influence of the surface electric field, New J. Phys. 21 (5) (2019) 053025.
[53] I. Mouton, Y. Chang, P. Chakraborty, S. Wang, L.T. Stephenson, T. Ben Britton, B. Gault, Hydride growth mechanism in zircaloy-4: investigation of the partitioning of alloying elements, Materialia (Oxf.) 15 (2021) 101006.
[54] P. Chemelle, D.B. Knorr, J.B. Van Der Sande, R.M. Pelloux, Morphology and composition of second phase particles in zircaloy-2, J. Nucl. Mater. 113 (1) (1983) 58–64.
[55] A. Etienne, B. Radiguet, N.J. Cunningham, G.R. Odette, P. Pareige, Atomic scale investigation of radiation-induced segregation in austenitic stainless steels, J. Nucl. Mater. 406 (2) (2010) 244–250.
[56] W.-Y. Chen, J.D. Poplawsky, Y. Chen, W. Guo, J.-W. Yeh, Irradiation-induced segregation at dislocation loops in CoCrFeMnNi high entropy alloy, Materialia (Oxf.) 14 (2020).
[57] T.P. Davis, M.A. Auger, C. Hofer, P.A.J. Bagot, M.P. Moody, D.E.J. Armstrong, Nanocluster evolution and mechanical properties of ion irradiated T91 ferritic-martensitic steel, J. Nucl. Mater. 548 (2021).
[58] C. Dai, F. Long, P. Saidi, L.K. Béland, Z. Yao, M.R. Daymond, Primary damage production in the presence of extended defects and growth of vacancy-type dislocation loops in hcp zirconium, Phys. Rev. Mater. 3 (4) (2019).
[59] C. Dai, P. Saidi, Z. Yao, M.R. Daymond, Atomistic simulations of Ni segregation to irradiation induced dislocation loops in Zr-Ni alloys, Acta Mater. 140 (2017) 56–66.
[60] D. Haley, P.A.J. Bagot, M.P. Moody, DF-fit: a robust algorithm for detection of crystallographic information in atom probe tomography data, microscopy and microanalysis, Off. J. Microsc. Soc. Am. Microb. Analy. Soc. Microscop. Soc. Can. 25 (2) (2019) 331–337.
[61] B.P. Geiser, T.F. Kelly, D.J. Larson, J. Schneir, J.P. Roberts, Spatial distribution maps for atom probe tomography, Microsc. Microanal. 13 (6) (2007) 437–447.
[62] M. Christensen, W. Wolf, C.M. Freeman, E. Wimmer, R.B. Adamson, L. Hallstadius, P.E. Cantonwine, E.V. Mader, Effect of alloying elements on the properties of Zr and the Zr–H system, J. Nucl. Mater. 445 (1–3) (2014) 241–250.

[63] M. Christensen, W. Wolf, C. Freeman, E. Wimmer, R.B. Adamson, M. Griffiths, E. V. Mader, Vacancy loops in breakaway irradiation growth of zirconium: insight from atomistic simulations, J. Nucl. Mater. 529 (2020).
[64] H. Okamoto, Sn-Zr (Tin-Zirconium), J. Phase Equilibria Diffus. 31 (4) (2010) 411–412.
[65] M. Griffiths, R.W. Gilbert, V. Fidleris, R.P. Tucker, R.B. Adamson, Neutron damage in zirconium alloys irradiated at 644 to 710 k, J. Nucl. Mater. 150 (2) (1987) 159–168.
[66] F. Garzarolli, P. Dewes, G. Maussner, H.H. Basso, Effects of high neutron fluences on microstructure and growth of zircaloy-4, in: L.F.P. Van Swam, C.M. Eucken (Eds.), Zirconium in the Nuclear Industry: Eighth International Symposium, ASTM International, West Conshohocken, PA, 1989, pp. 641–657.
[67] J.P. Abriata, J. Garcés, R. Versaci, The O−Zr, Oxygen-Zirconium) system, Bull. Alloy Phase Diagr. 7 (2) (1986) 116–124.
[68] N. Ni, S. Lozano-Perez, J. Sykes, C. Grovenor, Quantitative EELS analysis of zirconium alloy metal/oxide interfaces, Ultramicroscopy 111 (2) (2011) 123–130.
[69] Y. Dong, A.T. Motta, E.A. Marquis, Atom probe tomography study of alloying element distributions in Zr alloys and their oxides, J. Nucl. Mater. 442 (1–3) (2013) 270–281.
[70] P. Tejland, M. Thuvander, H.-O. Andrén, S. Ciurea, T. Andersson, M. Dahlbäck, L. Hallstadius, Detailed analysis of the microstructure of the metal/oxide interface region in zircaloy-2 after autoclave corrosion testing, J. ASTM. Int. 8 (6) (2011) 1–16.
[71] T. Ahmed, L.H. Keys, The breakaway oxidation of zirconium and its alloys a review, J. Less Common Metal. 39 (1) (1975) 99–107.
[72] K. Une, K. Nogita, S. Ishimoto, K. Ogata, Crystallography of Zirconium Hydrides in Recrystallized Zircaloy-2 Fuel Cladding by Electron Backscatter Diffraction, J. Nucl. Sci. Technol. 41 (7) (2004) 731–740.
[73] H. Khanchandani, A.A. El-Zoka, S.H. Kim, U. Tezins, D. Vogel, A. Sturm, D. Raabe, B. Gault, L.T. Stephenson, Laser-equipped gas reaction chamber for probing environmentally sensitive materials at near atomic scale, PLoS One 17 (2) (2022) e0262543.
[74] A.A. El-Zoka, L.T. Stephenson, S.H. Kim, B. Gault, D. Raabe, The fate of water in hydrogen-based iron oxide reduction, Adv. Sci. (Weinh.) 10 (24) (2023) e2300626.
[75] A. Saksena, B. Sun, X. Dong, H. Khanchandani, D. Ponge, B. Gault, Optimizing site-specific specimen preparation for atom probe tomography by using hydrogen for visualizing radiation-induced damage, Int. J. Hydrogen. Energy (2023).